Numerical simulation and performance optimization of a lead-free inorganic perovskite solar cell using SCAPS-1D

Sujan Banik, Arnob Das [*], Barun K. Das, Nurul Islam

Department of Mechanical Engineering, Rajshahi University of Engineering and Technology, Rajshahi-6204, Bangladesh

A R T I C L E   I N F O

A B S T R A C T

The perovskite solar cells, founded on lead halides, have garnered significant attention from the photovoltaic industry owing to their superior efficiency, ease of production, lightweight characteristics, and affordability. However, due to the hazardous nature of lead-based compounds, these solar cells are currently unsuitable for commercial production. In this context, a lead-free perovskite, cesium-bismuth iodide ($Cs_3Bi_2I_9$) is considered as a potential alternative to the lead halide-based cell due to their non-toxicity and stability, but this perovskite cannot be matched with random hole transport layer (HTL) and electron transport layer (ETL) materials compared to lead halide-based perovskite because of their crystal structure and band gap. Therefore, in this study, performance comparison of different ideal HTL and ETL materials for $Cs_3Bi_2I_9$ perovskite layer were studied using SCAPS-1D device simulation on the basis of open circuit voltage, short circuit current, power conversion efficiency (PCE) and fill factor (FF) as well as several novel PSC configuration models were designed that can direct for further experimental research for PSC device commercialization. Results from this investigation reveals that the maximum efficiency of 20.96 % is obtained for the configuration ITO/WS_2/$Cs_3Bi_2I_9$/NiO/Au with optimized parameters such as thickness 400 nm, band gap 2.1eV, absorber layer defect density 10^{12} cm^{-3}, donor density of ETL 10^{18} cm^{-3} and the acceptor density of HTL 10^{20} cm^{-3}.

1. Introduction

The consumption of power and energy is increasing with accelerated commercialization and industrialization [1]. The continuous utilization of conventional fuels such as natural gas, oils, hydrocarbon gas liquids, fossil fuels and the severe environmental effect for using these materials raises serious concerns about the research of alternate energy resources [2–4]. To replace the non-renewable energy resources and to fulfill the increasing energy demand in an environment friendly way, proper utilization of renewable energy sources is badly needed [5,6]. Solar power represents a promising renewable energy resource amidst various potential alternatives, including wind, geothermal, hydroelectric, oceanic, bio-based, and tidal sources. Notably, the production of solar cells has undergone substantial expansion in recent times, facilitated by a reduction in their cost. However, for solar energy to emerge as a significant energy source and rival fossil fuels, the expenses associated with solar cell production must be minimized. To achieve this goal, significant strides have been made in developing innovative cell materials, including the emergence of a new generation of perovskite solar cells (PSCs) that exhibit satisfactory performance metrics, and are poised for commercialization. These PSCs are projected to have a profound impact on the solar cell industry, given their low cost of raw materials and simple manufacturing process,

---

and they may even emerge as a competitive alternative to natural gas [7].

The solar research field have been recently captured by organic-inorganic PSCs due to having exceptional and excellent properties such as high absorptivity, low atomic energy, improved dielectric constant, favorable deposition by solution processing technique, high electron mobility, high hole mobility, suitable with low manufacturing cost and low-temperature deposition than conventional silicon-based solar cells [8,9]. The efficiency and stability of perovskites solar cells show tremendous improvement such as in just 10 years perovskite solar cells developed from unstable 3 % efficiency to stable 32 % efficiency and this improvement shows the potentiality of perovskite solar cells for which these solar cells have raised as strong competitor in the photovoltaic industry [10–12].

Thin-film PSC technology has improved due to the ease fabrication, energy gap adjustability, and the photon conversion efficiency (PCE) above 30 % of lead (Pb)-compounded organic inorganic halide PSCs [13]. Although these achievements, the existence of emerging contaminants (Pb) that causes toxicity is the fundamental issues in the applications of lead-based PSCs and this problem is still a significant barrier to commercialization of PSCs [14]. Furthermore, the organic constituents of the perovskite layer are a contributing factor to the instability of the solar cell. Correspondingly, the instability of the solar cell is attributed to the presence of organic constituents in the perovskite layer. Consequently, the deployment of lead-based organic halide perovskite solar cells is deemed inappropriate and inauspicious for industrial implementation and commercialization. To eliminate the toxicity researchers have carried out experiments to develop lead-free perovskite material and to minimize instability utilizing inorganic materials have gathered attractive attention which can replace organic materials [15–17]. Ahmad et al. simulated a $Cs_3Bi_2I_9$ based 2D PSC device where they employed TiO_2 as ETL material and Spiro-MeOTAD as HTL material with gold as back contact [18]. Their simulation results revealed that their PSC device could gain an efficiency of 11.54 % and their experimental results showed 1.66 % efficiency for the similar configuration. Researchers are also working on stabilizing experimented PSC devices against several influencing natural factors such as moisture, temperature and dust. Hamukwaya et al. [19] experimented to investigate the performance after adding KI as additive with $Cs_3Bi_2I_9$ perovskite layer. The highest efficiency was attained by the mixing of KI, resulting in a 2.81 % output. This was attributed to the stabilizing effect of the $Cs_3Bi_2I_9$ perovskite layer on the resultant PSC device against humidity. Remarkably, the PCE remained at 98 % of its initial value even after 90 days, indicating its suitability for solar cell applications.

Homo-valent component such as Ge^{2+} and Sn^{2+} can be a potential choice which can eliminate toxicity; however, these components decrease the stability of PSCs when it performs at ambient temperature [20–22]. For alternation of such materials different hetero-valent materials are tested in lab-based experiments to investigate their suitability and stability for using in perovskite layers and among those materials Bi^{3+} and Sb^{3+} which have stable +3 oxidation phase have gathered much attention [23]. Bi^{3+} has good optoelectronic properties as Pb^{2+} due to ionic radius and electronic structure similarities of these materials. Among different Bi halide-based materials $Cs_2Bi_2I_9$ achieved the greatest interest due to its higher PCE and more stability than other Bi based perovskite materials [24,25]. Summary of different works on the PSC performance analysis are listed in Table 1.

$Cs_3Bi_2I_9$ is a hybrid organic-inorganic perovskite material that has gained attention in the field of photovoltaics as a potential absorber layer in solar cells. This material has a range of advantages that make it an attractive candidate for this application. One of the significant advantages of $Cs_3Bi_2I_9$ is its high absorption coefficient. This characteristic enables it to absorb light effectively across a broad range of the solar spectrum, which is essential for the efficient operation of solar cells. The high absorption coefficient of $Cs_3Bi_2I_9$ is comparable to other well-known perovskite absorbers like $MAPbI_3$ (methylammonium lead iodide). Another advantage of $Cs_3Bi_2I_9$ is its high stability. Many perovskite materials are known to be unstable under ambient conditions, which can limit their practical applications. However, Cs3Bi2I9 has been shown to be highly stable under various environmental conditions, including humidity, light, and heat. This stability makes it an attractive option for use in real-world applications where stability is crucial. $Cs_3Bi_2I_9$ also has high carrier mobility, which is a desirable property for efficient charge transport and collection in photovoltaic devices. Furthermore, this material has a direct bandgap, which is crucial for efficient light absorption and conversion into electrical energy in photovoltaic devices [23].

In this study, the simulation has been carried out in two steps, where the first step consists of comparison of suitable ETL and HTL materials with $Cs_3Bi_2I_9$ absorber layer to find out the best configuration for which higher performance has been observed. In the second step, the selected model has been optimized for improving its performance parameters such as J_{sc}, V_{oc}, PCE and FF. To achieve the optimized system, around 45 models with different ETL and HTL materials have been performed. In this process, the best performance for $ITO/WS_2/Cs_3Bi_2I_9/NiO/Au$ has been attained. For further improvement of this configuration, optimization of various adjustable

Table 1
Literature review on recent experimental perovskite-based solar cells performance.

Device structure	Year	PCE(%)	V_{OC}(V)	J_{SC}(mA/cm^2)	FF(%)	Ref
Au/spiro-OMeTAD/FTO/TiO2	2022	12.54	1.32	13.13	72.01	[26]
HTL/back contact/MAPbBr$_3$/SnO$_2$/FTO	2021	25.40	1.19	25.09	84	[27]
Ag/BCP/PCBM/(Cs$_{0.05}$(FA5/MAI)$_{0.95}$Pb(I$_{0.9}$Br$_{0.1}$)$_3$)/PTAA/TTO/Glass	2021	23	1.16	24	82	[28]
Cu/BCP/ITUC$_{60}$/Cs$_{0.05}$(FA$_{0.92}$MA$_{0.08}$)$_{0.95}$Pb(I$_{0.92}$Br$_{0.08}$)$_3$/PTAA/ITO	2020	22.30	1.71	24.10	81	[29]
Au/Spiro-OMeTAD/CsSn$_{0.5}$Ge$_{0.5}$I$_3$/PCBM/FTO	2019	7.11	0.63	18.61	60.6	[30]
ITO/NiO$_x$/FASnI$_3$/PCBM/Ag	2018	6.70	0.60	17.53	65	[31]
Ag/PCBM/MASn$_{0.6}$Pb$_{0.4}$I$_{3-x}$Br$_x$/PEDOT:PSS/ITO	2017	12.10	0.78	20.65	75	[32]
Au/Spiro-OMeTAD/Cs$_{0.16}$FA$_{0.84}$Pb(I$_{0.88}$Br$_{0.12}$)$_3$/SnO$_2$/FTO	2016	18	1.02	22.40	78	[33]
Ag/BCP/PCBM/0.15 mol% Al$_3$+-dopedCH$_3$NH$_3$PbI$_3$/Poly-TPD/FTO	2016	19.10	1.01	22.40	78	[34]
Au/spiro-OMeTAD/MASnI$_3$/ZnO/ITO	2015	7.66	0.97	11.10	66	[35]
Au/SpiroOMeTAD + LiTFSI + tBP/MASnI$_3$/*m*-TiO$_2$/TiO$_2$	2014	6.40	0.88	16.80	42	[36]

attributes such as thickness and bandgap of absorber layer, defect density of absorber layer and charge carrier density of HTL and ETL materials has been done. After tuning input attributes, 20.96 % of PCE has been obtained for this model.

2. Model development and perovskite solar cell structure

2.1. Numerical modeling

In order to construct any form of a practical solar cell, numerical models have become a crucial tool. Perovskite solar cells' numerical modeling is a crucial technique for evaluating the validity of the proposed physical reasons and predicting the impact of physical modifications on cell performance [37]. Numerical modeling is required because perovskite solar cells are so complicated in their behavior [38].

Numerical simulation software offers useful information to select materials before experiment and commercialization. The One Dimension Solar Cell Capacitance Simulator (SCAPS-1D) program which is created by Burgelman et al. [39] can be used to do the numerical calculations of PSCs [40]. SCAPS-1D software solves the charge carrier continuity Equations such as hole continuity Equation (1) and electron continuity Equation (2), the semiconductor Poisson Equation (3) in one direction, total charge transport Equation (4), electron transport Equation (5), hole transport Equation (6) and optical absorption coefficient Equation (7).

$$\frac{dn_p}{dt} = G_n - \frac{n_p - n_{p0}}{\tau_n} + n_p \mu_n \frac{d\xi}{dx} + \mu_n \xi \frac{dn_p}{ds} + D_n \frac{d^2 n_p}{dx^2} \tag{1}$$

$$\frac{dn_n}{dt} = G_p - \frac{p_n - p_{n0}}{\tau_p} + p_n \mu_p \frac{d\xi}{dx} + \mu_p \xi \frac{dn_n}{ds} + D_p \frac{d^2 p_n}{dx^2} \tag{2}$$

$$\frac{d^2 \varnothing(x)}{dx^2} = \frac{q}{\epsilon_o \epsilon_r} \left(p(x) - n(x) + N_D - N_A + -0.3\rho_p - -0.3\rho_n \right) \tag{3}$$

$$J = J_n + J_p \tag{4}$$

$$J_n = D_n \frac{dn}{dx} + \mu_n n \frac{d\varphi}{dx} \tag{5}$$

$$J_p = D_p \frac{dp}{dx} + \mu_p p \frac{d\varphi}{dx} \tag{6}$$

$$\alpha(\lambda) = \left(A + \frac{B}{hv} \right) \sqrt{hv - E_g} \tag{7}$$

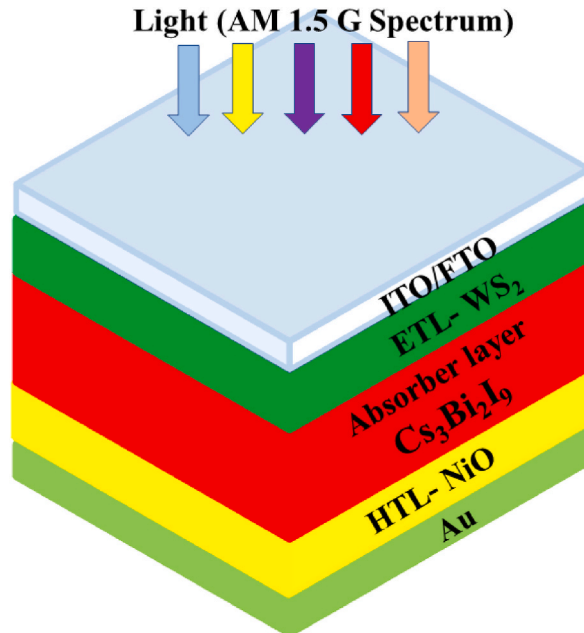Fig. 1. Model of a perovskite-based solar cell with different layers.

where, ξ is the electric field, q denotes electrical charge whose typical value is considered as 1.602×10^{-19} C, ϵ_o is the vacuum absolute permittivity and ϵ_r is the semiconductor relative permittivity, N_D and N_A represent donor doping density and acceptor doping density respectively, p(x) and n(x) are carrier density of hole and electron, $-0.3\,\rho_p$ is the defect density of hole and $-0.3\,\rho_n$ is the defect density of electron, G_n and G_p indicates electron generation rate and hole generation rate respectively, J_n and J_p are current density and hole current density of electron, respectively, μ_n and μ_p are electron and hole mobilities, τ_n and τ_p represents lifetime of electrons and holes respectively, D_p and D_n represents diffusion coefficient of free hole and electron. v represents optical frequency, A and B depicts arbitrary constant while E_g represents bandgap, h represents plank constant and $\alpha(\lambda)$ depicts absorption coefficient. More information about these equations can be learned from somewhere [41–45].

2.2. PSC structure and material characteristics

2.2.1. PSC structure

The device structure in this paper is Au/HTL/absorber layer/ETL/ITO/glass, where Au is employed as back contact having work function of 5.1eV and $Cs_3Bi_2I_9$ is applied as absorber or perovskite layer. The simulation is carried out with different ETLs and HTLs to obtain a novel optimized configuration. The ETLs that are simulated in this study include TiO_2, PCBM, WS_2, IGZO and C60 whereas CuO, Cu_2O, PEDOT:PSS, P3HT, CuSCN, $CuSbS_2$, NiO, Spiro-OMeTAD and CuI are applied as hole transport layer material.

Fig. 1 shows a typical model of PSC with different layers such as ITO, ETL, absorber layer and HTL.

The band diagram of our selected configuration is showed in Fig. 2, from where it can be seen that the blue curve depicts the conduction band line and red curve shows the valence band line.

2.2.2. Physical input parameters and methodology

The AM1.5 illumination spectrum is used by default in this study. The incident light power (Ps) and temperature are fixed at 1000 W/m^2 and 300 K, respectively. In every layer, the thermal velocities of the electrons and holes are fixed at 10^7 cm/s. The absorption co-efficient (α) of ETL and HTL layers are determined in SCAPS-1D through Equation (8) [46], like in many works on PSCs,
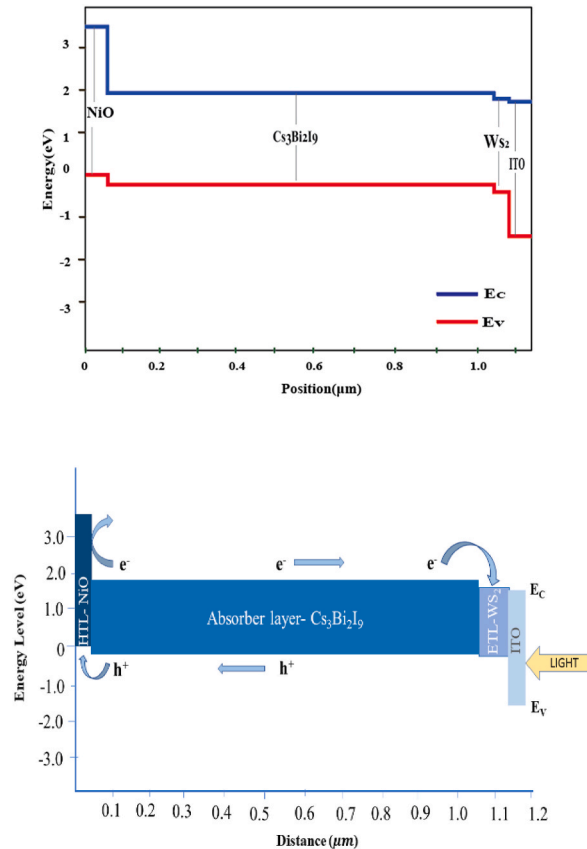
$$\alpha = A_a \sqrt{(hv - E_g)} \tag{8}$$

Fig. 2. Energy band diagram for the selected configuration in this study.

where, A_a is a layer-dependent pre-factor in the simulation. The application of interface defects has schemed the design more realistic and assisted to predict the experimental behavior of the solar cell model.

PSC device investigation has been carried out in two different steps where the first step includes building up a PSC device configuration with suitable HTL and ETL for $Cs_3Bi_2I_9$ absorber layer. Different input attributes for nine HTL materials have been listed in Table 2 and input parameters for five ETL materials have been listed in Table 3. With these various ETL and HTL materials 45 different configurations have been simulated. After scrutinized comparison, it was found that when WS_2 as ETL and NiO as HTL were applied as charge transporting layers then the configuration ($ITO/WS_2/Cs_3Bi_2I_9/NiO/Au$) showed best results with higher performance parameters. In the second stage, the selected model ($ITO/WS_2/Cs_3Bi_2I_9/NiO/Au$) has been optimized by tuning bandgap and thickness of absorber layer, defect density of absorber layer and carrier density of ETL and HTL.

3. Results and discussion

3.1. Optimization of ETL and HTL

In this study, $Cs_3Bi_2I_9$ was selected as absorber layer due to its non-toxicity and better optoelectronic parameter, however it's hard enough to match this absorber layer with appropriate ETL and HTL due to band structure of $Cs_3Bi_2I_9$. To obtain the best performance, simulation of the configuration ($ITO/ETL/Cs_3Bi_2I_9/HTL/Au$) for five different ETL materials and nine different HTL materials have been carried out.

Fig. 3 shows performance parameters of different PSC configurations for different HTLs where PCBM and $Cs_3Bi_2I_9$ were applied as ETL and absorber layer respectively. In a similar way, Fig. 4 shows performance parameters for WS_2 ETL, Fig. 5 shows comparison for IGZO ETL, Fig. 6 reveals performance comparison for C60 ETL as well as comparison for TiO_2 ETL can be observed in Fig. 7. After scrutinized comparison, it can be observed from these figures that when NiO and WS_2 were applied as HTL and ETL, respectively, the configuration $ITO/WS_2/Cs_3Bi_2I_9/NiO/Au$ shows best performance characteristics. The optimized characteristics are given in Table 4 for which improved performance characteristics were obtained. From Figs. 4–7, it can be observed that the maximum 20.25 % PCE can be achieved when WS_2 and NiO were employed as ETL and HTL material respectively with $Cs_3Bi_2I_9$ perovskite layer. Cu_2O also showed extraordinary performance with WS_2 ETL and $Cs_3Bi_2I_9$ absorber layer. However, as the configuration $ITO/WS_2/Cs_3Bi_2I_9/NiO/Au$ shows best performance so further optimization was carried out for this model.

3.2. Effect of absorber layer thickness

The light-absorbing layer thickness has a great impact on the performance of PSCs. The layer needs an optimized thickness for the collection of solar radiation basically to collect photons and facilitate the electron and hole pair generation. The photon absorption density drops hence the efficiency when there is a decrease in layer thickness from the optimized value [67]. And with the augmentation of thickness the photon absorption falls down because of the recombination of electron hole pair [68]. In this paper, the thickness of $Cs_3Bi_2I_9$ was varied from 400 to 5000 nm for getting optimized thickness for the model. There was a change in V_{OC}, J_{SC}, FF and PCE with the variation in absorber layer thickness. These changes have been graphically represented on Fig. 8 (i) and (ii).

Firstly, it has been observed that with the extension of absorber layer thickness, the V_{OC} decreases from 1.4368 to 1.4279 V. The reason behind this is the recombination of charge carrier for their longer travel path. However, the J_{SC} has increased with the increase in absorber layer thickness. This is because of the rise in the spectral response when wavelength is longer. On the contrary the FF got reduced from 84.85 % to 72.06 % and the reason is the enhancement of series resistance and might be because of the charge carrier recombination along with the resistant losses. The maximum value of PCE was found 20.59 % for the thickness of 400 nm which was taken as optimum thickness. For further augmentation of thickness there was a drop in PCE. This is because of the charge pathway resistance and enhanced radiative recombination [69].

Table 2
Input attributes for perovskite material, different electron transport layer (ETL) materials and ITO.

Parameter	$Cs_3Bi_2I_9$ [47]	PCBM [48,49]	TiO_2 [50–52]	WS_2 [53]	IGZO [48]	C60 [54]	ITO [55]
Electron affinity, X (eV)	3.40	3.90	4.26	3.95	4	3.90	4.1
Relative permittivity (ε_r)	9.68	4	100	13.60	9	4.20	10
Thickness (nm)	1000	30	30	100	30	50	60
Bandgap, E_g (eV)	2.1	2	3.20	1.80	3.50	1.70	3.6
State density of conduction band, N_C (1/cm^3)	4.98×10^{19}	1×10^{21}	2×10^{18}	10^7	5×10^{18}	8.0×10^{19}	2.2×10^{18}
State density of valence band, N_V (1/cm^3)	2.11×10^{19}	2×10^{20}	1.8×10^{19}	10^7	5×10^{18}	8.0×10^{19}	1.8×10^{19}
AL defect density, N_t (1/cm^3)	10^{14}	1×10^{14}	1×10^{14}	10^{15}	1×10^{15}	1×10^{14}	–
Mobility of electron, μ_n (cm^2/Vs)	10^7	1×10^{-2}	2×10^4	100	15	8.0×10^{-2}	10^7
Mobility of hole, μ_p (cm^2/Vs)	10^7	1×10^{-2}	1×10^3	100	0.20	3.5×10^{-3}	10^7
AD, NA (1/cm^3)	10^{19}	–	–	–	–	–	–
DD, ND (1/cm^3)	10^{19}	1×10^{20}	6×10^{19}	10^{18}	1×10^{17}	2.6×10^{17}	10^{19}

Table 3

Input attributes for different hole transport layer (HTL) materials.

Parameter	NiO [49]	CuO [56]	Cu$_2$O [57]	PEDOT [58]	P3HT [57]	CuSCN [57]	CuI [59–62]	Spiro-OMeTAD [63]	CuSbS$_2$ [64–66]
Relative permittivity (ε_r)	11.75	18.1	7.1	3	3	10	6.5	3	14.6
Bandgap, Eg (eV)	3.6	31.5	2.17	3.6	1.7	3.4	2.98	2.9	1.58
Electron affinity, X (eV)	2.1	4.07	3.2	1.57	3.5	2.1	2.1	2.2	4.2
Thickness (nm)	50	50	50	50	50	50	50	350	50
AL defect density, N_t (1/cm^3)	1×10^8	1×10^{13}	1×10^{13}	1×10^{14}	1×10^{14}	1×10^8	1×10^{15}	1×10^{13}	1×10^{18}
State density of conduction band, N_C (1/cm^3)	2.5×10^{20}	2.2×10^{19}	2.5×10^{20}	2.2×10^{18}	2×10^{18}	2.5×10^{18}	2.8×10^{19}	2.5×10^{18}	2×10^{18}
State density of valence band, N_V (1/cm^3)	2.5×10^{20}	5.5×10^{20}	2.5×10^{20}	1.8×10^{19}	2×10^{19}	1.8×10^{19}	1×10^{19}	1.8×10^{19}	1×10^{18}
Mobility of electron, μ_n (cm^2/Vs)	1×10^{-3}	100	200	100	1.8×10^{-3}	2×10^{-4}	1.69×10^{-4}	2×10^{-4}	49
Mobility of hole, μ_p (cm^2/Vs)	1×10^{-3}	0.1	8600	4	1.8×10^{-2}	2×10^{-4}	1.69×10^{-4}	2×10^{-4}	49
AD, NA (1/cm^3)	1×10^{19}	1×10^{15}	1×10^{19}	2×10^{19}	1×10^{18}	1×10^{17}	1×10^{18}	1×10^{17}	1×10^{18}
DD, ND (1/cm^3)	–	–	–	–	–	–	–	–	–

	NiO	Cu2O	CuO	PEDOT	P3HT	CuSCN	Spiro	CuI	CuSbS2
Voc (V)	1.463	1.459	1.478	1.4628	1.405	1.463	1.4585	1.4623	1.461
Jsc (mA/cm2)	10.698	10.706	10.694	10.699	10.89	10.698	10.74	10.699	10.698
FF (%)	84.53	84.27	83.04	84.58	79.76	84.38	85.45	82.4	84.33
PCE (%)	13.23	13.17	12.86	13.24	12.22	13.21	13.4	12.89	13.18

Fig. 3. Performance parameters for different HTLs with PCBM ETL and Cs3Bi2I9 absorber layer.

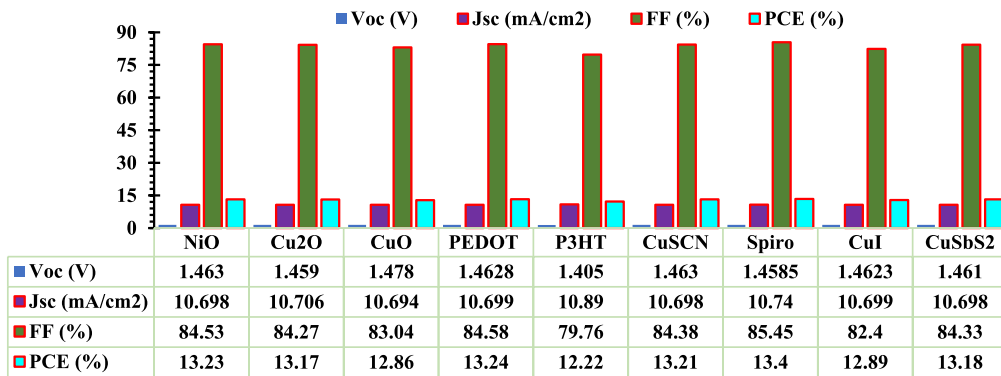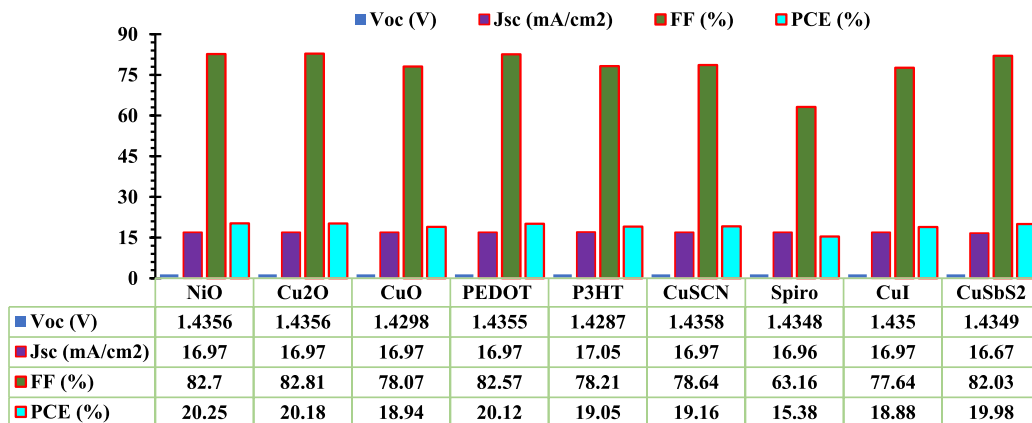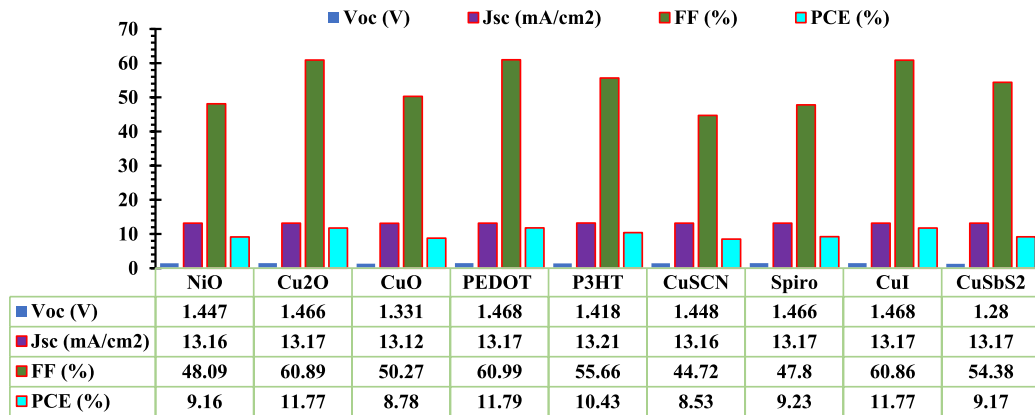|	NiO	Cu2O	CuO	PEDOT	P3HT	CuSCN	Spiro	CuI	CuSbS2
Voc (V)	1.4356	1.4356	1.4298	1.4355	1.4287	1.4358	1.4348	1.435	1.4349
Jsc (mA/cm2)	16.97	16.97	16.97	16.97	17.05	16.97	16.96	16.97	16.67
FF (%)	82.7	82.81	78.07	82.57	78.21	78.64	63.16	77.64	82.03
PCE (%)	20.25	20.18	18.94	20.12	19.05	19.16	15.38	18.88	19.98

Fig. 4. Performance parameters for different HTLs with WS$_2$ ETL and Cs3Bi2I9 absorber layer.

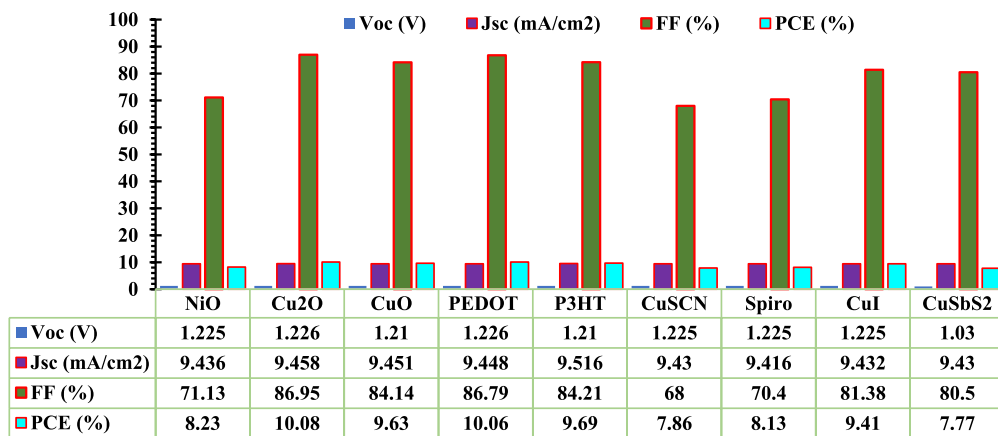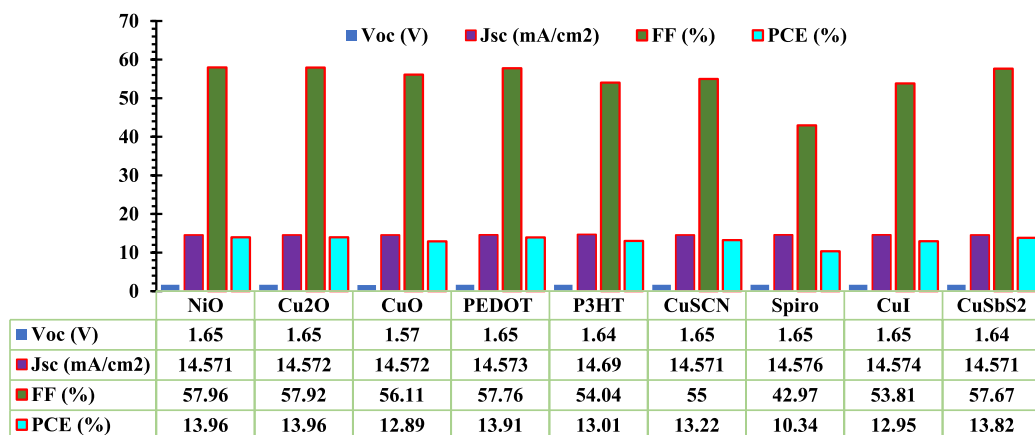**Fig. 5.** Performance parameters for different HTLs with IGZO ETL and Cs3Bi2I9 absorber layer.

	NiO	Cu2O	CuO	PEDOT	P3HT	CuSCN	Spiro	CuI	CuSbS2
■ Voc (V)	1.447	1.466	1.331	1.468	1.418	1.448	1.466	1.468	1.28
■ Jsc (mA/cm2)	13.16	13.17	13.12	13.17	13.21	13.16	13.17	13.17	13.17
■ FF (%)	48.09	60.89	50.27	60.99	55.66	44.72	47.8	60.86	54.38
□ PCE (%)	9.16	11.77	8.78	11.79	10.43	8.53	9.23	11.77	9.17

Fig. 6. Performance parameters for different HTLs with C60 ETL and Cs3Bi2I9 absorber layer.

	NiO	Cu2O	CuO	PEDOT	P3HT	CuSCN	Spiro	CuI	CuSbS2
■ Voc (V)	1.225	1.226	1.21	1.226	1.21	1.225	1.225	1.225	1.03
■ Jsc (mA/cm2)	9.436	9.458	9.451	9.448	9.516	9.43	9.416	9.432	9.43
■ FF (%)	71.13	86.95	84.14	86.79	84.21	68	70.4	81.38	80.5
□ PCE (%)	8.23	10.08	9.63	10.06	9.69	7.86	8.13	9.41	7.77

Fig. 7. Performance parameters for different HTLs with TiO$_2$ ETL and Cs3Bi2I9 absorber layer.

	NiO	Cu2O	CuO	PEDOT	P3HT	CuSCN	Spiro	CuI	CuSbS2
■ Voc (V)	1.65	1.65	1.57	1.65	1.64	1.65	1.65	1.65	1.64
■ Jsc (mA/cm2)	14.571	14.572	14.572	14.573	14.69	14.571	14.576	14.574	14.571
■ FF (%)	57.96	57.92	56.11	57.76	54.04	55	42.97	53.81	57.67
□ PCE (%)	13.96	13.96	12.89	13.91	13.01	13.22	10.34	12.95	13.82

Table 4
Optimized input attributes for the selected configuration in this study.

Parameters	ITO	WS$_2$	Cs$_3$Bi$_2$I$_9$	NiO
Electron affinity (eV)	4.1	3.95	3.4	2.1
Bandgap (eV)	3.6	1.8	**2.10**	3.6
Thickness (nm)	60	100	**400**	150
Dielectric permittivity (relative)	10	13.6	9.68	11.75
Thermal velocity of hole (cm/s)	10^7	10^7	10^7	10^7
Mobility of electron (cm^2/Vs)	50	100	4.3	10^{-3}
CB effective density of states (cm^{-3})	2.2×10^{18}	2×10^{18}	4.98×10^{19}	2.5×10^{20}
VB effective density of states (cm^{-3})	1.8×10^{19}	2×10^{18}	2.11×10^{19}	2.5×10^{20}
Thermal velocity of electron (cm/s)	10^7	2×10^5	10^7	10^7
Mobility of hole (cm^2/Vs)	75	100	1.7	10^{-3}
Shallow uniform DD, N$_D$ (cm^{-3})	10^{19}	**10^{18}**	10^{19}	-
Shallow uniform AD, N$_A$ (cm^{-3})	–	–	10^{19}	**1×10^{20}**
Defect density of AL, N$_t$ (cm^{-3})	–	10^{13}	**10^{12}**	1×10^{14}

Note: The bold attributes depict the optimized input parameters.
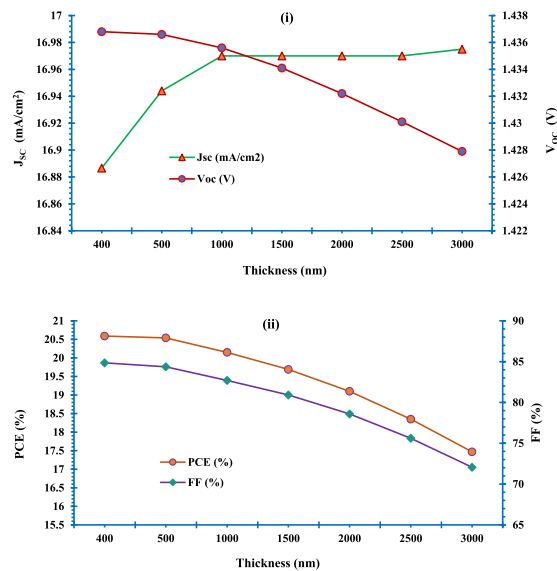
Fig. 8. Effect of absorber layer thickness on PSC device' performance parameters (i). (J$_{sc}$, V$_{oc}$), and (ii) (FF, PCE).

3.3. Effect of absorber layer band gap

The absorber layer band gap is an pivotal parameter for the absorber layer, and it possesses a major influence on the effectiveness of the PSCs. In this regard, tunability is the most important property of PSCs. The energy gap of perovskite absorber is tuned from 1.65 eV to 2.34 eV to investigate the performance of the PSC. Fig. 9 (i) and (ii) reported that the maximum value of V$_{OC}$ 1.4669V is obtained at 2.34 eV, J$_{SC}$ of 22.88 mA/cm^2 at 1.65 eV, and the maximum PCE and FF of the device were found 20.9 % and 88.79 %, respectively at 2.1 eV.

The FF and PCE increased from 63.87 % to 88.79 % and 19.16 %–20.9 % with the augmentation of bandgap from 1.65 to 2.1 eV. After there was a decrease in FF and PCE with increase in band gap because of lowering the band gap increases the number of electrons but the problem is the energy of the electrons wasted as heat energy. On the other hand, higher the band gap the generation of electrons drops for some of the photon's higher energy [70]. The optimum value of bandgap was taken 2.1 eV for the maximum PCE of 20.9 %.

3.4. Effect of defect density of the absorber layer

In order to attain the stable PV output parameters, the proper amount of defect density is important. The defect density impacts directly on the recombination and generation of electron hole pairs which also has an impact on the efficiency of the PSCs [71]. Defect density depends on the quality of the absorber layer. If the quality is poor, then this causes higher defect density. For this reason, recombination of electron hole pair increases hence reduce the efficiency of the perovskite film.

The recombination rate is contingent upon the diffusion length, which itself is influenced by the bulk defect density of the PSC. In
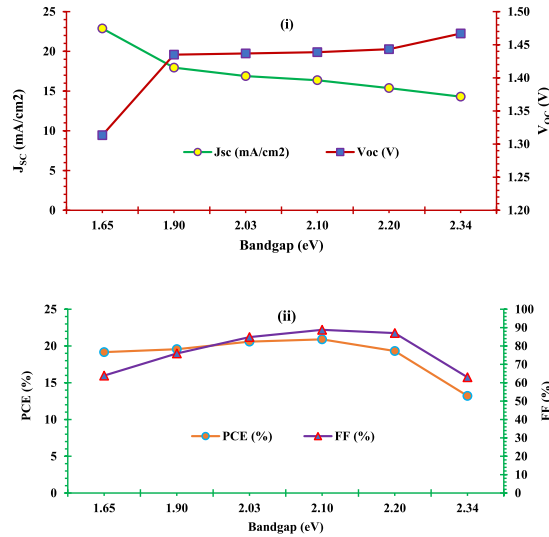
Fig. 9. Effect of absorber layer bandgap on (i) Jsc, Voc, and (ii) FF, PCE.

PSCs, Shockley-Read-Hall (SRH) recombination reigns supreme, and the determination of diffusion length can be achieved through the utilization of the trap assisted SRH recombination model [72]. The following two Equations (9) and (10) is used to describe SRH recombination.

$$R_{SRH} = \frac{np - n_{i^2}}{\left[\pi\left(p + n + \frac{2n_i \, \cosh(E_i - E_t)}{kT}\right)\right]} \tag{9}$$

$$\tau = \frac{1}{[\sigma \times N_t \times V_{th}]} \tag{10}$$

where, τ represents the lifetime of charge carriers, σ is the capture cross section of charge carriers, N_t is the defect density of the perovskite absorber layer, V_{th} is the thermal velocity of charge carriers.

The diffusion length, $L = \sqrt{D\tau}$, where $D = \frac{kT}{e}\mu$. Here, D refers to the diffusion coefficient and τ refers to the lifetime of minority carriers. In addition to that k denotes as Boltzmann's constant, e refers to the charge of electron, T refers to the temperature, and μ denotes as mobility of charge carrier.
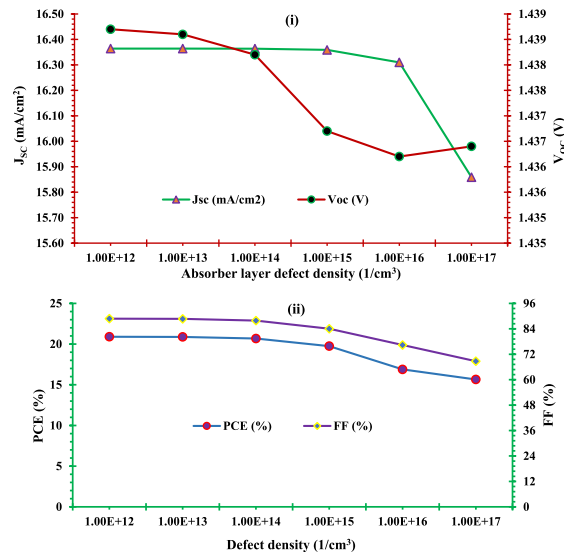
Fig. 10. Effect of absorber layer defect density on (i) Jsc, Voc, and (ii) FF, PCE.

The defect density has an impact on the value of V_{OC} by the following Equation (11).

$$V_{oc} = \frac{kT}{q} \ln\left(\frac{J_{sc}}{J_o} + 1\right) \tag{11}$$

where, J_O and J_{SC} represent the recombination current density and short-circuit current density, respectively.

In order to get the optimum defect density, N_t of the absorber layer on the PSCs performance is analyzed by taking the values from 10^{12} cm^{-3} to 10^{17} cm^{-3}. Fig. 10 (i) and (ii) show that with the increase in defect density all the photovoltaic parameters decrease. The V_{OC} drops from 1.4387 V to 1.4364 V and the J_{sc} from 16.364 to 15.859 mA/cm^2. A high density of defects can lead to a decrease in V_{OC} due to the increase in recombination. In devices with high defect densities, the recombination rate becomes dominant, leading to a decrease in V_{OC}. In addition, the increase in defect density can lead to an increase in the trap-assisted recombination rate, which can also reduce the V_{OC} of the device. The values PCE and FF remains almost similar up to the defect density of 10^{12} cm^{-3} to 10^{14} cm^{-3} and reduce significantly after 10^{15} cm^{-3}. Therefore, the optimal defect density is taken as 10^{12} cm^{-3}. The maximum PCE and FF is found to be 20.9 % and 88.79 % respectively for the defect density of 10^{-12} cm^{-3}.

3.5. Effect of carrier density

The doping of both the electron transport layer (ETL) and the hole transport layer (HTL) may be achieved through one of two distinct methods. One such method involves the utilization of minority carriers to facilitate the doping rate. However, this method results in a significant reduction in the photovoltaic characteristics of the system. Conversely, doping with majority carriers, which exhibit notably enhanced PV attributes, may also be employed. It is noteworthy that an intermediate level of doping density can lead to an improved performance of the perovskite solar cell (PSC).

3.5.1. Effect of donor density of ETL

In order to find the best suitable doping concentration of ETL, the donor density for WS$_2$ was enhanced from 10^{15} cm^{-3} to 10^{19} cm^{-3}. The variation of V_{oc}, J_{sc}, FF and the PCE was shown in Fig. 11 (i) and (ii). The PCE and FF increased from 19.88 % to 20.96 % and 82.53 %–89.03 %, respectively with the increase in donor density from 10^{15} to 10^{18} cm^{-3}. The J_{sc} was almost constant with the variation and there was a sudden drop after 10^{18} cm^{-3}. Additionally, the V_{oc} enhanced from 1.43V to 1.44V with the rise in doping concentration. The optimal value of donor density was taken as 10^{18} cm^{-3} as the maximum PCE 20.96 % was found at that value. The higher value of N_D makes it easy to extract charge and transportation of charge at the ETL/perovskite interface [73].

3.5.2. Effect of acceptor density of HTL

The variation of acceptor density of HTL(N_A) has a major influence on the performance of PSCs. The small amount of variation in acceptor concentration caused variation in the stability of the PSCs. To obtain the optimum value of N_A, the N_A was varied from 10^{16} cm^{-3} to 10^{20} cm^{-3}. There was a small increase in V_{oc} and J_{sc} from 1.4385V to 1.4388V and 16.359 mA/cm^2 to 16.366 mA/cm^2 with the increase in HTL acceptor density (Fig. 12 (i)).

In addition to that the PCE and FF were improved from 20.26 % to 20.96 % and 86.11 %–89.03 %, respectively with the augmentation of N_A (Fig. 12 (ii)). Therefore, the optimum value of N_A was taken 10^{20} cm^{-3} as the maximum PCE 20.96 % was found at that value of acceptor concentration. The higher the N_A, the production of interface electric field among the PSC layer is higher. It causes the increase in electric potential. However, this growth in PCE brings a higher recombination of charge carriers, which causes an increase in dopant concentration in the absorber layer [73,74].

3.6. Comparison of initial and optimized final model

An improvement of current-voltage characteristic can be seen from Fig. 13 for the optimized final model than the initial model. From the J-V characteristic curve, performance parameters of a PSC device can be understood. Here, from the J-V curve it can be observed that for the final optimized model an improved I–V curve is obtained than that of initial model.

Fig. 14 depicts that the quantum efficiency in optimized final model is higher than the quantum efficiency of initial model. To obtain proper knowledge about quantum efficiency of the initial model and optimized final model, the wavelength varied from 300 nm to 900 nm. In this wavelength range, the quantum efficiency varied due to tuning of different input attributes such as bandgap and thickness of absorber layer, carrier density and defect density of absorber material.

Quantum efficiency (QE) measures a solar cell's capacity to produce charge carriers from photon energy. From Fig. 14, it's clear that higher quantum efficiency can be obtained by tuning the PSC device in a proper way, thus higher amount of charge carriers can be produced from the absorber layer, that means generation rate would be increased. As a result, better performance can be obtained due greater generation of electron-hole pairs.

3.7. Comparison with literature

Organic spiro-OMeTAD can be fabricated in flexible and simple method of manufacture, therefore, is the material that is most frequently employed in the commercial and industrial sectors [75]. Despite this, the material is unsuitable for PSCs due to poor hole mobility, low conductivity, high manufacturing costs, and instability brought on by moisture, oxidation, and light. Additionally, TiO$_2$
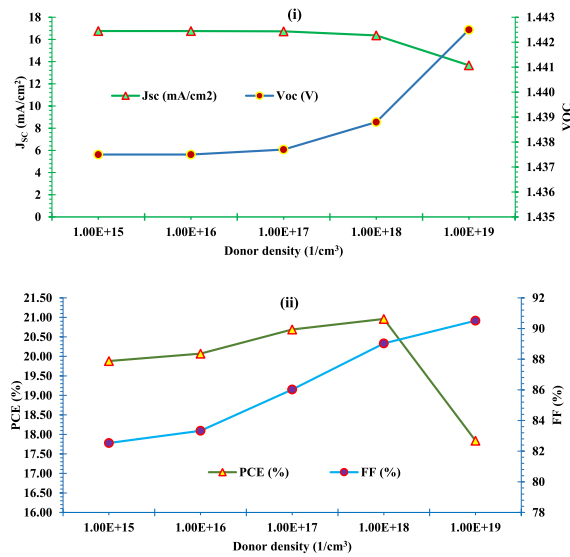
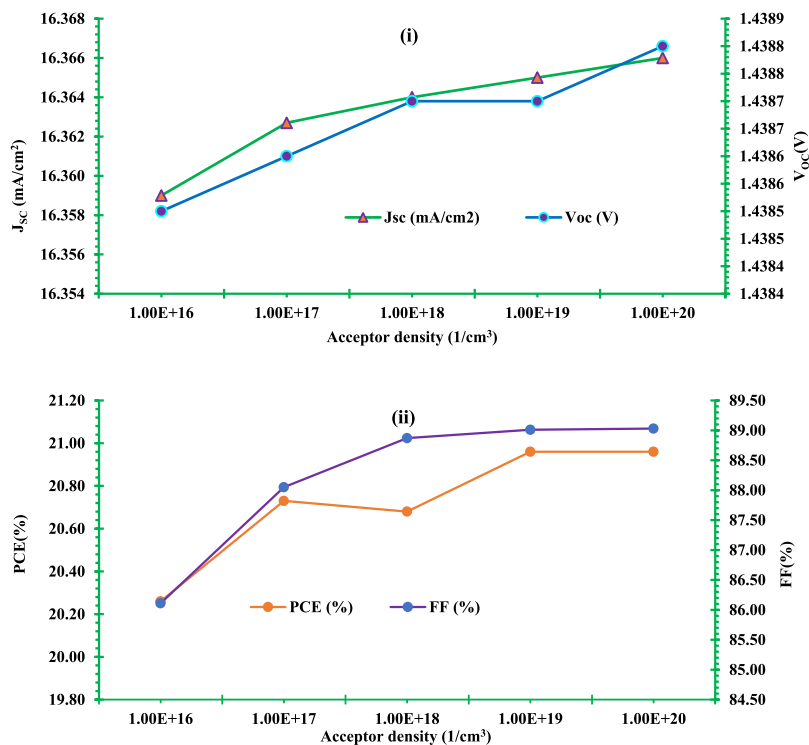**Fig. 11.** Effect of donor density of ETL (WS$_2$) on (i) Jsc, Voc, and (ii) FF, PCE.

Fig. 12. Effect of acceptor density of HTL(NiO) on (i) Jsc, Voc, and (ii) FF, PCE.

is another popular n-type material which is most commonly used as ETL. Despite having potential for excellent photovoltaic function, photo corrosion resistance, superior thermal stability, and the 3.2eV bandgap presents a difficulty [76]. PSC configurations with these materials and lead-based perovskite shows better characteristics that is clear from table, however due to their toxicity and instability problem further improvement are required through investigating new materials to replace these toxic and unstable materials.

In this study, a novel PSC model was designed and simulated that shows better performance characteristics after optimization which can be seen from Table 5. Additionally, the selected perovskite material (Cs$_3$Bi$_2$I$_9$) is considered much stable [84] which is introduced in the previous section. Therefore, the designed model in this present work can be considered for further experiment and
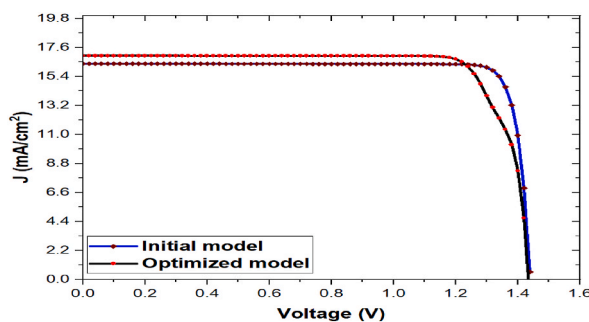
Fig. 13. Comparison of J-V characteristic curve of initial and final optimized model.
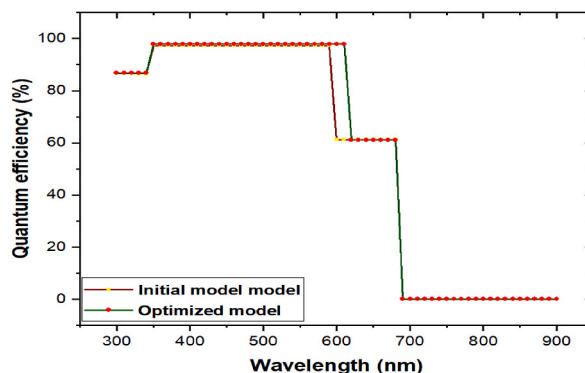

Fig. 14. Comparison of capacitance of initial and final optimized model as a function of wavelength.

Table 5

Comparison of different established model with the present model in this study.

Models	Methods	V_{OC}(V)	J_{SC}(mA/cm^2)	FF(%)	PCE(%)	Ref
FTO/TiO2/Cs$_3$Sb$_2$I$_9$/spiro-OMeTAD/Au	Simulation	1.32	13.13	72.01	12.54	[26]
CZTSe/MAPbI$_3$/Cd$_{1-x}$Zn$_x$S/FTO	Simulation	1.12	26.45	88.90	27.13	[77]
PTAA/MAPbI$_3$/TiO$_2$	Experimental	1.11	19.58	76	16.46	[78]
Spiro − OMeTAD/MAPbI$_3$/TiO$_2$	Simulation	1.27	21.87	79.58	22.13	[79]
Spiro − OMeTAD/MAPbI$_3$/TiO$_2$	Experimental	1.09	23.83	76.2	19.71	[80]
CuI/MAPbI$_3$/TiO$_2$	Simulation	1.27	21.89	83.12	23.14	[79]
CuI/MAPbI$_3$/TiO$_2$	Experimental	0.55	17.8	62	6	[81]
NiO$_x$/MAPbI$_3$/PCBM: C$_{60}$/Zr	Experimental	1.08	23.47	79.4	20.13	[82]
FTO/TiO2/Cs3Bi2I9/spiro-MeOTAD/Au	Simulation	1.03	21.02	73.4	11.14	[83]
FTO/TiO$_2$/Cs$_3$Bi$_2$I$_9$/NiO	Simulation	0.92	22.07	68.21	13.82	[83]
ITO/WS$_2$/Cs$_3$Bi$_2$I$_9$/NiO/Au	Simulation	1.438	16.366	89.03	20.96	[Present work]

commercialization.

4. Conclusions

In this paper, the modeling and performance analysis was done for the Cs$_3$Bi$_2$I$_9$ based PSC using SCAPS-1D. The lead-free Cs$_3$Bi$_2$I$_9$ was used as the absorber layer and the selection of this layer was based on the better stability and non-toxicity of this material. WS$_2$, PCBM, C60, TiO$_2$, IGZO were used as the ETL material and Cu$_2$O, CuSCN, CuSbS$_2$, P3HT, PEDOT:PSS, Spiro-OMeTAD, NiO, CuI, CuO was used as the HTL material. Total of 45 different PSC models were simulated with the combination of these HTL and ETL with the Cs$_3$Bi$_2$I$_9$ based absorber layer. In addition, Au was taken as the back contact material. After the numerical simulation of these models, the combination of WS$_2$–Cs$_3$Bi$_2$I$_9$–NiO was found to give the maximum PCE of 20.25 %. This combination is the novel model in which WS$_2$ is used as ETL with Cs$_3$Bi$_2$I$_9$ perovskite layer. In order to enhance the performance parameters (V$_{OC}$, Jsc, FF, PCE) of the PSC and to achieve the maximum PCE, this model was scrutinized by varying the parameters like absorber layer thickness, band gap, defect density and carrier density of the ETL and HTL. The thickness of absorber layer was found to be 400 nm as optimum as PCE was maximum 20.59 % at 400 nm. Thin absorber layer was found to give the good efficiency for the perovskite model. There was a significant change in the performance with the variation of absorber layer band gap. For the band gap of 2.1 eV, the PCE was the highest

among others. There was found a significant increase in PCE from 20.59 % to 20.9 % for this bandgap. Though, the defect density has a major impact on the effectiveness of the PSCs, there was observed no such changes in the maximum efficiency with the variation of defect density. The maximum efficiency of 20.9 % was found at the absorber layer dopant density of 10^{12} cm^{-3}. There was a gradual increase in the performance parameters with the variation in carrier density. The maximum of 20.96 % PCE was obtained with the ETL donor density of 10^{18} cm^{-3} which was the best we found in our numerical analysis. Since, higher the N$_D$ makes the extraction of the charge easier to the ETL/perovskite layer. The optimum acceptor density of HTL was found to be 10^{20} cm^{-3} and here also the maximum PCE was found to be 20.96 %. Finally, after the full optimization the PSC attained a PCE of 20.96 % which was initially found to be 20.25 %.

Data availability statement

Data is available in this article.

Additional information

No additional information is available for this paper.

CRediT authorship contribution statement

Sujan Banik: Writing – review & editing, Writing – original draft, Software, Methodology, Conceptualization. **Arnob Das:** Writing – review & editing, Writing – original draft, Validation, Supervision, Software, Resources, Methodology, Investigation, Formal analysis, Conceptualization. **Barun K. Das:** Writing – review & editing, Writing – original draft, Visualization, Supervision, Investigation, Conceptualization. **Nurul Islam:** Visualization, Supervision.

Declaration of competing interest

The authors declare that they have no known competing financial interests or personal relationships that could have appeared to influence the work reported in this paper.

Acknowledgement

References

[1] Susmita Datta Peu, et al., A comprehensive review on recent advancements in absorption-based post combustion carbon capture technologies to obtain a sustainable energy sector with clean environment, Sustainability 15 (7) (2023) 5827, https://doi.org/10.3390/su15075827.

[2] W. Azam, I. Khan, S.A. Ali, Alternative energy and natural resources in determining environmental sustainability: a look at the role of government final consumption expenditures in France, Environ. Sci. Pollut. Control Ser. 30 (1) (2023 Jan) 1949–1965, https://doi.org/10.1007/s11356-022-22334-z.

[3] D.A. Tofu, K. Wolka, T. Woldeamanuel, The impact of alternative energy technology investment on environment and food security in northern Ethiopia, Sci. Rep. 12 (2022) 1, https://doi.org/10.1038/s41598-022-14521-2, 2022;12:1–11.

[4] A. Das, S.D. Peu, A comprehensive review on recent advancements in thermochemical processes for clean hydrogen production to decarbonize the energy sector, Sustainability 14 (2022) 11206, https://doi.org/10.3390/SU141811206, 2022;14:11206.

[5] A. Das, S.D. Peu, MdS. Hossain, M.A.M. Akanda, M.M. Salah, M.M.H. Akanda, et al., Metal oxide nanosheet: synthesis approaches and applications in energy storage devices (batteries, fuel cells, and supercapacitors), Nanomaterials 13 (2023) 1066, https://doi.org/10.3390/NANO13061066, 2023;13:1066.

[6] A. Das, S. Datta Peu, M. Abdul Mannan Akanda, et al., Peer-to-Peer energy trading pricing mechanisms: towards a comprehensive analysis of energy and network service pricing (NSP) mechanisms to get sustainable enviro-economical energy sector, Energies 16 (2023) 2198, https://doi.org/10.3390/EN16052198, 2023;16:2198.

[7] S. Ma, G. Yuan, Y. Zhang, N. Yang, Y. Li, Q. Chen, Development of encapsulation strategies towards the commercialization of perovskite solar cells, Energy Environ. Sci. 15 (2022) 13–55, https://doi.org/10.1039/D1EE02882K.

[8] Y.H. Kim, H. Cho, J.H. Heo, T.S. Kim, N.S. Myoung, C.L. Lee, et al., Multicolored organic/inorganic hybrid perovskite light-emitting diodes, Adv. Mater. 27 (2015) 1248–1254, https://doi.org/10.1002/ADMA.201403751.

[9] L. Dou, Y.M. Yang, J. You, Z. Hong, W.H. Chang, G. Li, et al., Solution-processed hybrid perovskite photodetectors with high detectivity, Nat. Commun. 5 (2014) 1–6, https://doi.org/10.1038/ncomms6404, 1 2014;5.

[10] A. Kojima, K. Teshima, Y. Shirai, T. Miyasaka, Organometal halide perovskites as visible-light sensitizers for photovoltaic cells, J. Am. Chem. Soc. 131 (2009) 6050–6051, https://doi.org/10.1021/JA809598R/SUPPL_FILE/JA809598R_SI_001.PDF.

[11] M. Ameri, M. Ghaffarkani, R.T. Ghahrizjani, N. Safari, E. Mohajerani, Phenomenological morphology design of hybrid organic-inorganic perovskite solar cell for high efficiency and less hysteresis, Sol. Energy Mater. Sol. Cell. 205 (2020) 110251, https://doi.org/10.1016/J.SOLMAT.2019.110251.

[12] T. Xiang, Y. Zhang, H. Wu, J. Li, L. Yang, K. Wang, et al., Universal defects elimination for high performance thermally evaporated CsPbBr3 perovskite solar cells, Sol. Energy Mater. Sol. Cell. 206 (2020) 110317, https://doi.org/10.1016/J.SOLMAT.2019.110317.

[13] H. Bi, G. Han, M. Guo, C. Ding, H. Zou, Q. Shen, et al., Multistrategy preparation of efficient and stable environment-friendly lead-based perovskite solar cells, ACS Appl. Mater. Interfaces 14 (2022) 35513–35521, https://doi.org/10.1021/ACSAMI.2C06032/SUPPL_FILE/AM2C06032_SI_006.MP4.

[14] K. Shivesh, I. Alam, A.K. Kushwaha, M. Kumar, S.V. Singh, Investigating the theoretical performance of Cs2TiBr6-based perovskite solar cell with La-doped BaSnO3 and CuSbS2 as the charge transport layers, Int. J. Energy Res. 46 (2022) 6045–6064, https://doi.org/10.1002/ER.7546.

[15] Z. Shi, J. Guo, Y. Chen, Q. Li, Y. Pan, H. Zhang, et al., Lead-free organic–inorganic hybrid perovskites for photovoltaic applications: recent advances and perspectives, Adv. Mater. 29 (2017) 1605005, https://doi.org/10.1002/ADMA.201605005.

[16] M.I. Ustinova, S.D. Babenko, S.Y. Luchkin, F.S. Talalaev, D.v. Anokhin, S. Olthof, et al., Experimental evaluation of indium(I) iodide as a lead-free perovskite-inspired material for photovoltaic applications, J Mater Chem C Mater 10 (2022) 3435–3439, https://doi.org/10.1039/D1TC05583F.

[17] L. Romani, A. Speltini, C.N. Dibenedetto, A. Listorti, F. Ambrosio, E. Mosconi, et al., Experimental strategy and mechanistic view to boost the photocatalytic activity of Cs3Bi2Br9 lead-free perovskite derivative by g-C3N4 composite engineering, Adv. Funct. Mater. 31 (2021) 2104428, https://doi.org/10.1002/ADFM.202104428.

[18] K. Ahmad, M.Q. Khan, R.A. Khan, H. Kim, Numerical simulation and fabrication of Pb-free perovskite solar cells (FTO/TiO2/Cs3Bi2I9/spiro-MeOTAD/Au), Opt. Mater. 128 (2022) 112458, https://doi.org/10.1016/j.optmat.2022.112458.

[19] S.L. Hamukwaya, H. Hao, M.M. Mashingaidze, T. Zhong, S. Tang, J. Dong, J. Xing, H. Liu, Potassium iodide-modified lead-free Cs3Bi2I9 perovskites for enhanced high-efficiency solar cells, Nanomaterials 12 (21) (2022) 3751, https://doi.org/10.3390/nano12213751.

[20] T.M. Koh, T. Krishnamoorthy, N. Yantara, C. Shi, W.L. Leong, P.P. Boix, et al., Formamidinium tin-based perovskite with low Eg for photovoltaic applications, J Mater Chem A Mater 3 (2015) 14996–15000, https://doi.org/10.1039/C5TA00190K.

[21] N.K. Noel, S.D. Stranks, A. Abate, C. Wehrenfennig, S. Guarnera, A.A. Haghighirad, et al., Lead-free organic–inorganic tin halide perovskites for photovoltaic applications, Energy Environ. Sci. 7 (2014) 3061–3068, https://doi.org/10.1039/C4EE01076K.

[22] T. Krishnamoorthy, H. Ding, C. Yan, W.L. Leong, T. Baikie, Z. Zhang, et al., Lead-free germanium iodide perovskite materials for photovoltaic applications, J Mater Chem A Mater 3 (2015) 23829–23832, https://doi.org/10.1039/C5TA05741H.

[23] A. Das, S.D. Peu, M.A.M. Akanda, M.M. Salah, M.S. Hossain, B.K. Das, Numerical simulation and optimization of inorganic lead-free Cs3Bi2I9-based perovskite photovoltaic cell: impact of various design parameters, Energies 16 (2023) 2328, https://doi.org/10.3390/EN16052328, 2023;16:2328.

[24] A.J. Lehner, D.H. Fabini, H.A. Evans, C.A. Hébert, S.R. Smock, J. Hu, et al., Crystal and electronic structures of complex bismuth iodides A3Bi2I9 (A = K, Rb, Cs) related to perovskite: aiding the rational design of photovoltaics, Chem. Mater. 27 (2015) 7137–7148, https://doi.org/10.1021/ACS.CHEMMATER.5B03147/SUPPL_FILE/CM5B03147_SI_001.PDF.

[25] B.W. Park, B. Philippe, X. Zhang, H. Rensmo, G. Boschloo, E.M.J. Johansson, Bismuth based hybrid perovskites A3Bi2I9 (A: methylammonium or cesium) for solar cell application, Adv. Mater. 27 (2015) 6806–6813, https://doi.org/10.1002/ADMA.201501978.

[26] K. Ahmad, M.Q. Khan, H. Kim, Simulation and fabrication of all-inorganic antimony halide perovskite-like material based Pb-free perovskite solar cells, Opt. Mater. 128 (2022) 112374, https://doi.org/10.1016/j.optmat.2022.112374.

[27] X. Feng, Q. Guo, J. Xiu, Z. Ying, K.W. Ng, L. Huang, et al., Close-loop recycling of perovskite solar cells through dissolution-recrystallization of perovskite by butylamine, Cell Rep Phys Sci 2 (2021) 100341, https://doi.org/10.1016/J.XCRP.2021.100341.

[28] S. Cacovich, G. Vidon, M. Degani, M. Legrand, L. Gouda, J.B. Puel, et al., Imaging and quantifying non-radiative losses at 23% efficient inverted perovskite solar cells interfaces, Nat. Commun. 13 (2022) 1, https://doi.org/10.1038/s41467-022-30426-0, 2022;13:1–9.

[29] X. Zheng, Y. Hou, C. Bao, J. Yin, F. Yuan, Z. Huang, et al., Managing grains and interfaces via ligand anchoring enables 22.3%-efficiency inverted perovskite solar cells, Nat. Energy (2020 5) 131–140, https://doi.org/10.1038/s41560-019-0538-4, 2 2020;5.

[30] M. Chen, M.G. Ju, H.F. Garces, A.D. Carl, L.K. Ono, Z. Hawash, et al., Highly stable and efficient all-inorganic lead-free perovskite solar cells with native-oxide passivation, Nat. Commun. 10 (2019) 1–8, https://doi.org/10.1038/s41467-018-07951-y, 1 2019;10.

[31] Q. Tai, X. Guo, G. Tang, P. You, T.W. Ng, D. Shen, et al., Antioxidant grain passivation for air-stable tin-based perovskite solar cells, Angew. Chem. Int. Ed. 58 (2019) 806–810, https://doi.org/10.1002/ANIE.201811539.

[32] S. Lee, D.W. Kang, Highly efficient and stable Sn-rich perovskite solar cells by introducing bromine, ACS Appl. Mater. Interfaces 9 (2017) 22432–22439, https://doi.org/10.1021/ACSAMI.7B04011/SUPPL_FILE/AM7B04011_SI_001.PDF.

[33] M. Fievez, P.J. Singh Rana, T.M. Koh, M. Manceau, J.H. Lew, N.F. Jamaludin, et al., Slot-die coated methylammonium-free perovskite solar cells with 18% efficiency, Sol. Energy Mater. Sol. Cell. (2021) 230, https://doi.org/10.1016/J.SOLMAT.2021.111189.

[34] J.T.W. Wang, Z. Wang, S. Pathak, W. Zhang, D.W. Dequilettes, F. Wisnivesky-Rocca-Rivarola, et al., Efficient perovskite solar cells by metal ion doping, Energy Environ. Sci. 9 (2016) 2892–2901, https://doi.org/10.1039/C6EE01969B.

[35] U. Bansode, R. Naphade, O. Game, S. Agarkar, S. Ogale, Hybrid perovskite films by a new variant of pulsed excimer laser deposition: a roomerature dry process, J. Phys. Chem. C 119 (2015) 9177–9185, https://doi.org/10.1021/ACS.JPCC.5B02561/SUPPL_FILE/JP5B02561_SI_001.PDF.

[36] N.K. Noel, S.D. Stranks, A. Abate, C. Wehrenfennig, S. Guarnera, A.A. Haghighirad, et al., Lead-free organic–inorganic tin halide perovskites for photovoltaic applications, Energy Environ. Sci. 7 (2014) 3061–3068, https://doi.org/10.1039/C4EE01076K.

[37] C. Doroody, K.S. Rahman, T.S. Kiong, N. Amin, Optoelectrical impact of alternative window layer composition in CdTe thin film solar cells performance, Sol. Energy 233 (2022) 523–530, https://doi.org/10.1016/J.SOLENER.2022.01.049.

[38] C. Zuo, L. Ding, Solution-Processed Cu2O and CuO as hole transport materials for efficient perovskite solar cells, Small 11 (2015) 5528–5532, https://doi.org/10.1002/SMLL.201501330.

[39] M. Burgelman, P. Nollet, S. Degrave, Modelling polycrystalline semiconductor solar cells, Thin Solid Films 361–362 (2000) 527–532, https://doi.org/10.1016/S0040-6090(99)00825-1.

[40] M. Burgelman, P. Nollet, S. Degrave, Modelling polycrystalline semiconductor solar cells, Thin Solid Films 361–362 (2000) 527–532, https://doi.org/10.1016/S0040-6090(99)00825-1.

[41] M. Burgelman, K. Decock, S. Khelifi, A. Abass, Advanced electrical simulation of thin film solar cells, Thin Solid Films 535 (2013) 296–301, https://doi.org/10.1016/J.TSF.2012.10.032.

[42] Z. Xiao, Y. Yuan, Q. Wang, Y. Shao, Y. Bai, Y. Deng, et al., Thin-film semiconductor perspective of organometal trihalide perovskite materials for high-efficiency solar cells, Mater. Sci. Eng. R Rep. 101 (2016) 1–38, https://doi.org/10.1016/J.MSER.2015.12.002.

[43] M. Burgelman, J. Verschraegen, S. Degrave, P. Nollet, Modeling thin-film PV devices, Prog. Photovoltaics Res. Appl. 12 (2004) 143–153, https://doi.org/10.1002/PIP.524.

[44] J. Verschraegen, M. Burgelman, Numerical modeling of intra-band tunneling for heterojunction solar cells in scaps, Thin Solid Films 515 (2007) 6276–6279, https://doi.org/10.1016/J.TSF.2006.12.049.

[45] S.A. Moiz, A.N.M. Alahmadi, A.J. Aljohani, Design of a novel lead-free perovskite solar cell for 17.83% efficiency, IEEE Access 9 (2021) 54254–54263, https://doi.org/10.1109/ACCESS.2021.3070112.

[46] K. Sobayel, M. Akhtaruzzaman, K.S. Rahman, M.T. Ferdaous, Z.A. Al-Mutairi, H.F. Alharbi, et al., A comprehensive defect study of tungsten disulfide (WS2) as electron transport layer in perovskite solar cells by numerical simulation, Results Phys. 12 (2019) 1097–1103, https://doi.org/10.1016/J.RINP.2018.12.049.

[47] M.T. Islam, M.R. Jani, K.M. Shorowordi, Z. Hoque, A.M. Gokcek, V. Vattipally, S.S. Nishat, S. Ahmed, Numerical simulation studies of Cs3Bi2I9 perovskite solar device with optimal selection of electron and hole transport layers, Optik 231 (2021) 166417, https://doi.org/10.1016/j.ijleo.2021.166417.

[48] N. Lakhdar, A. Hima, Electron transport material effect on performance of perovskite solar cells based on CH3NH3GeI3, Opt. Mater. 99 (2020) 109517, https://doi.org/10.1016/J.OPTMAT.2019.109517.

[49] Y. Wang, Z. Xia, Y. Liu, H. Zhou, Simulation of perovskite solar cells with inorganic hole transporting materials, in: 2015 IEEE 42nd Photovoltaic Specialist Conference, PVSC 2015, 2015, https://doi.org/10.1109/PVSC.2015.7355717.

[50] M.D. Stamate, On the dielectric properties of dc magnetron TiO2 thin films, Appl. Surf. Sci. 218 (2003) 318–323, https://doi.org/10.1016/S0169-4332(03)00624-X.

[51] A. Niemegeers, M. Burgelman, Numerical modelling of ac-characteristics of CdTe and CIS solar cells, Conf. Rec. IEEE Photovolt. Spec. Conf. (1996), https://doi.org/10.1109/PVSC.1996.564274, 901–4.

[52] A. Husainat, W. Ali, P. Cofie, J. Attia, J. Fuller, Simulation and analysis of methylammonium lead iodide (CH3NH3PbI3) perovskite solar cell with Au contact using SCAPS 1D simulator. https://doi.org/10.11648/J.AJOP.20190702.12, 2019.

[53] K. Sobayel, M. Akhtaruzzaman, K.S. Rahman, M.T. Ferdaous, Z.A. Al-Mutairi, H.F. Alharbi, et al., A comprehensive defect study of tungsten disulfide (WS2) as electron transport layer in perovskite solar cells by numerical simulation, Results Phys. 12 (2019) 1097–1103, https://doi.org/10.1016/J.RINP.2018.12.049.

[54] K. Wojciechowski, T. Leijtens, S. Siprova, C. Schlueter, M.T. Hörantner, J.T.W. Wang, et al., C60 as an efficient n-type compact layer in perovskite solar cells, J. Phys. Chem. Lett. 6 (2015) 2399–2405, https://doi.org/10.1021/ACS.JPCLETT.5B00902/SUPPL_FILE/JZ5B00902_SI_001.PDF.

[55] A.M. Islam, S. Islam, K. Sobayel, E.I. Emon, F.A. Jhuma, M. Shahiduzzaman, M. Akhtaruzzaman, N. Amin, M.J. Rashid, Performance analysis of tungsten disulfide (WS2) as an alternative buffer layer for CdTe solar cell through numerical modeling, Opt. Mater. 120 (2021) 111296, https://doi.org/10.1016/j.optmat.2021.111296.

[56] C. Zuo, L. Ding, Solution-Processed Cu2O and CuO as hole transport materials for efficient perovskite solar cells, Small 11 (2015) 5528–5532, https://doi.org/10.1002/SMLL.201501330.

[57] Y. Raoui, H. Ez-Zahraouy, N. Tahiri, O. el Bounagui, S. Ahmad, S. Kazim, Performance analysis of MAPbI3 based perovskite solar cells employing diverse charge selective contacts: simulation study, Sol. Energy 193 (2019) 948–955, https://doi.org/10.1016/J.SOLENER.2019.10.009.

[58] M.H. Kumar, S. Dharani, W.L. Leong, P.P. Boix, R.R. Prabhakar, T. Baikie, et al., Lead-free halide perovskite solar cells with high photocurrents realized through vacancy modulation, Adv. Mater. 26 (2014) 7122–7127, https://doi.org/10.1002/ADMA.201401991.

[59] D. Chen, Y. Wang, Z. Lin, J. Huang, X. Chen, D. Pan, et al., Growth strategy and physical properties of the high mobility p-type cui crystal, Cryst. Growth Des. 10 (2010), https://doi.org/10.1021/CG100270D/SUPPL_FILE/CG100270D_SI_001.PDF, 2057–60.

[60] G. Hodes, Perovskite-based solar cells, Science (1979) 342 (2013) 317–318, https://doi.org/10.1126/SCIENCE.1245473.

[61] D. Liu, M.K. Gangishetty, T.L. Kelly, Effect of CH3NH3PbI3 thickness on device efficiency in planar heterojunction perovskite solar cells, J Mater Chem A Mater 2 (2014) 19873–19881, https://doi.org/10.1039/C4TA02637C.

[62] H. Wu, L.S. Wang, A study of nickel monoxide (NiO), nickel dioxide (ONiO), and Ni(O2) complex by anion photoelectron spectroscopy, J. Chem. Phys. 107 (1998) 16, https://doi.org/10.1063/1.474362.

[63] R. Hock, T. Mayer, W. Jaegermann, P-type doping of spiro-MeOTAD with WO 3 and the spiro-MeOTAD/WO 3 interface investigated by synchrotron-induced photoelectron spectroscopy, J. Phys. Chem. C 116 (2012) 18146–18154, https://doi.org/10.1021/JP301179V/ASSET/IMAGES/MEDIUM/JP-2012-01179V_0019.GIF.

[64] H.-J. Du(杜静静),) W-C Wang(王韦超, J.-Z. Zhu(朱键卓), H.-J. Du(杜会静),) W-C Wang(王韦超, J.-Z. Zhu(朱键卓), Device simulation of lead-free CH3NH3SnI3 perovskite solar cells with high efficiency, Chin. Phys. B 25 (2016), https://doi.org/10.1088/1674-1056/25/10/108802, 108802–108802.

[65] F. Anwar, R. Mahbub, S.S. Satter, S.M. Ullah, Effect of different HTM layers and electrical parameters on ZnO nanorod-based lead-free perovskite solar cell for high-efficiency performance, Int. J. Photoenergy 2017 (2017), https://doi.org/10.1155/2017/9846310.

[66] M. Ameri, E. Mohajerani, M. Ghafarkani, N. Safari, S.A. Alavi, The investigation of the unseen interrelationship of grain size, ionic defects, device physics and performance of perovskite solar cells, J. Phys. D Appl. Phys. 52 (2019) 125501, https://doi.org/10.1088/1361-6463/AAFEA9.

[67] A. Bag, R. Radhakrishnan, R. Nekovei, R. Jeyakumar, Effect of absorber layer, hole transport layer thicknesses, and its doping density on the performance of perovskite solar cells by device simulation, Sol. Energy 196 (2020) 177–182, https://doi.org/10.1016/J.SOLENER.2019.12.014.

[68] L. Lin, L. Jiang, P. Li, B. Fan, Y. Qiu, A modeled perovskite solar cell structure with a Cu2O hole-transporting layer enabling over 20% efficiency by low-cost low-temperature processing, J. Phys. Chem. Solid. 124 (2019) 205–211, https://doi.org/10.1016/J.JPCS.2018.09.024.

[69] I. Alam, M.A. Ashraf, Effect of Different Device Parameters on Tin-Based Perovskite Solar Cell Coupled with In2S3 Electron Transport Layer and CuSCN and Spiro-OMeTAD Alternative Hole Transport Layers for High-Efficiency Performance, 2020, https://doi.org/10.1080/15567036.2020.1820628.

[70] Sadanand, D.K. Dwivedi, Modeling of photovoltaic solar cell based on CuSbS absorber for the enhancement of performance, IEEE Trans Electron Devices 68 (2021) 1121–1128, https://doi.org/10.1109/TED.2020.3048326.

[71] Y. He, L. Xu, C. Yang, X. Guo, S. Li, Design and numerical investigation of a lead-free inorganic layered double perovskite Cs4CuSb2Cl12 nanocrystal solar cell by SCAPS-1D, Nanomaterials 11 (2021) 2321, https://doi.org/10.3390/NANO11092321, 2021;11:2321.

[72] Y. Chen, H. Shen, P.P. Altermatt, Analysis of recombination losses in screen-printed aluminum-alloyed back surface fields of silicon solar cells by numerical device simulation, Sol. Energy Mater. Sol. Cell. 120 (2014) 356–362, https://doi.org/10.1016/J.SOLMAT.2013.05.051.

[73] A. Mohandes, M. Moradi, H. Nadgaran, Numerical simulation of inorganic Cs2AgBiBr6 as a lead-free perovskite using device simulation SCAPS-1D, Opt. Quant. Electron. 53 (2021) 6, https://doi.org/10.1007/S11082-021-02959-Z, 2021;53:1–22.

[74] M.M. Salah, A. Abouelatta, A. Shaker, K.M. Hassan, A. Saeed, A comprehensive simulation study of hybrid halide perovskite solar cell with copper oxide as HTM, Semicond. Sci. Technol. 34 (2019) 115009, https://doi.org/10.1088/1361-6641/AB22E1.

[75] I. Alam, R. Mollick, M.A. Ashraf, Numerical simulation of Cs2AgBiBr6-based perovskite solar cell with ZnO nanorod and P3HT as the charge transport layers, Physica B Condens Matter 618 (2021) 413187, https://doi.org/10.1016/J.PHYSB.2021.413187.

[76] T. Ghrib, N.K. AL-Saleem, A. AL-Naghmaish, A.A. Elshekhipy, S. Brini, K. Briki, et al., Annealing effect on the microstructural, optical, electrical, and thermal properties of Cu2O/TiO2/Cu2O/TiO2/Si heterojunction prepared by sol-gel technique, Micro and Nanostructures 164 (2022) 107119, https://doi.org/10.1016/J.SPMI.2021.107119.

[77] Y.H. Khattak, E. Vega, F. Baig, B.M. Soucase, Performance investigation of experimentally fabricated lead iodide perovskite solar cell via numerical analysis, Mater. Res. Bull. 151 (2022) 111802, https://doi.org/10.1016/J.MATERRESBULL.2022.111802.

[78] Y.J. Jeon, S. Lee, R. Kang, J.E. Kim, J.S. Yeo, S.H. Lee, et al., Planar heterojunction perovskite solar cells with superior reproducibility, Sci. Rep. 4 (2014) 1–7, https://doi.org/10.1038/srep06953, 1 2014;4.

[79] F. Azri, A. Meftah, N. Sengouga, A. Meftah, Electron and hole transport layers optimization by numerical simulation of a perovskite solar cell, Sol. Energy 181 (2019) 372–378, https://doi.org/10.1016/J.SOLENER.2019.02.017.

[80] N. Ahn, D.Y. Son, I.H. Jang, S.M. Kang, M. Choi, N.G. Park, Highly reproducible perovskite solar cells with average efficiency of 18.3% and best efficiency of 19.7% fabricated via lewis base adduct of lead(II) iodide, J. Am. Chem. Soc. 137 (2015) 8696–8699, https://doi.org/10.1021/JACS.5B04930/SUPPL_FILE/JA5B04930_SI_001.PDF.

[81] J.A. Christians, R.C.M. Fung, P v Kamat, An inorganic hole conductor for Organo-lead halide perovskite solar cells. improved hole conductivity with copper iodide, J. Am. Chem. Soc. 136 (2014) 758–764, https://doi.org/10.1021/JA411014K/SUPPL_FILE/JA411014K_SI_001.PDF.

[82] H. Zhang, X. Ren, X. Chen, J. Mao, J. Cheng, Y. Zhao, et al., Improving the stability and performance of perovskite solar cells via off-the-shelf post-device ligand treatment, Energy Environ. Sci. 11 (2018) 2253–2262, https://doi.org/10.1039/C8EE00580J.

[83] M.T. Islam, M.R. Jani, K.M. Shorowordi, Z. Hoque, A.M. Gokcek, V. Vattipally, S.S. Nishat, S. Ahmed, Numerical simulation studies of Cs3Bi2I9 perovskite solar device with optimal selection of electron and hole transport layers, Optik 231 (2021) 166417, https://doi.org/10.1016/j.ijleo.2021.166417.

[84] D.K. Chaudhary, A. Sharma, A. Kumar, U. Chauhan, Bhasker DrHariP, DrPK. Dhawan, et al., Solvent engineering of Cs3bi2i9 perovskite films for lead-free flexible semi-transparent perovskite solar cell devices with enhanced efficiency, SSRN Electron. J. (2022), https://doi.org/10.2139/SSRN.4226736.